Keplerian Radial-Velocity Fitting for Single-Planet Exoplanet Parameter Estimation

Mauricio Tedeschi

July 11, 2026

Abstract

The radial-velocity (RV) method remains one of the foundational techniques for detecting and characterizing extrasolar planets. We present a compact, reproducible pipeline for estimating the orbital parameters of a single companion from Doppler time series. The forward model is the standard Keplerian RV curve parameterized by semi-amplitude K, period P, eccentricity e, argument of periastron ω, time of periastron t_0, and systemic velocity γ. Parameters are recovered with a global differential-evolution search followed by local nonlinear least-squares refinement. From the fitted amplitude and an assumed stellar mass we derive a minimum planet mass and orbital semi-major axis under the edge-on inclination limit. Synthetic experiments recover planted values of K and P to within a few percent at residual RMS of $\sim 2\,\mathrm{m\,s^{-1}}$. Application to four observational Doppler-shift series recovers a range of orbital architectures, including a short-period, nearly circular solution (`star0`: $P \approx 4.27\,\mathrm{d}$, $K \approx 56.7\,\mathrm{m\,s^{-1}}$, $M_p \sin i \approx 0.49\,M_J$) as well as longer-period companions. A velocity-Verlet two-body integration is used only for post-fit orbit visualization.

1 Introduction

The discovery of 51 Pegasi b established Doppler spectroscopy as a practical route to detecting planets around solar-type stars [1, 2]. In the RV method, the star and planet orbit their common barycenter; the line-of-sight component of the stellar motion appears as a periodic Doppler shift in the stellar spectrum. Modern surveys and modeling frameworks treat this signal with analytic Keplerian orbits and statistically motivated fitting procedures [3–5].

For a single planet on a Keplerian orbit, the stellar radial velocity is fully specified by a small set of orbital elements [6, 7]. The semi-amplitude K encodes the planet-to-star mass ratio and orbital scale, while P and e control the periodicity and waveform shape. Because the likelihood surface can be multimodal—especially when eccentricity and phase are free—global optimization or Bayesian sampling is often preferred over purely local gradient methods [8, 9].

This work implements a transparent single-planet RV estimator intended for reproducible analysis and pedagogical demonstration. The pipeline (i) converts Doppler shifts to radial velocities, (ii) fits a Keplerian model with differential evolution plus least-squares polish, and (iii) derives physical parameters and a barycentric orbit visualization. We validate the method on synthetic data with known ground truth and apply it to an observational Doppler time series.

2 Methods

2.1 Doppler shift and radial velocity

Spectroscopic observations may be reported as a fractional Doppler shift $z = \Delta\lambda/\lambda$. For a source with line-of-sight speed v relative to the observer, the relativistic Doppler formula is

$$z = \sqrt{\frac{1+\beta}{1-\beta}} - 1, \qquad \beta = \frac{v}{c}, \tag{1}$$

where c is the speed of light [10]. Inverting this relation yields

$$v = c\,\frac{(1+z)^2 - 1}{(1+z)^2 + 1}. \tag{2}$$

Throughout, positive v denotes recession.

2.2 Keplerian radial-velocity model

We adopt the standard single-planet RV model [3, 7]:

$$v_r(t) = \gamma + K\Big[\cos\big(\omega + \nu(t)\big) + e\cos\omega\Big], \tag{3}$$

where γ is the systemic velocity, K is the RV semi-amplitude, e is the eccentricity, ω is the argument of periastron, and $\nu(t)$ is the true anomaly.

The true anomaly is obtained from the mean anomaly

$$M = \frac{2\pi}{P}\,(t - t_0) \tag{4}$$

by solving Kepler's equation

$$E - e\sin E = M \tag{5}$$

for the eccentric anomaly E, then converting

$$\tan\frac{\nu}{2} = \sqrt{\frac{1+e}{1-e}}\,\tan\frac{E}{2} \tag{6}$$

[6]. Here P is the orbital period and t_0 is a time of periastron passage. Supplementary notation, unit conventions, and the visualization equations are collected in Appendix A.

For an edge-on orbit ($\sin i = 1$), the semi-amplitude is related to the component masses and period by

$$K = \left(\frac{2\pi G}{P}\right)^{1/3} \frac{M_p}{(M_\star + M_p)^{2/3}}\,\frac{1}{\sqrt{1-e^2}}, \tag{7}$$

where G is Newton's constant, i is the orbital inclination to the sky plane, $M_\star$ is the stellar mass, and M_p is the planet mass. When evaluating Eq. (7) numerically we convert P to seconds so that the combination is dimensionally consistent in SI units. Given K, P, e, and $M_\star$, we solve Eq. (7) for M_p and obtain the relative orbital semi-major axis from Kepler's third law,

$$a^3 = \frac{G(M_\star + M_p)}{4\pi^2}\,P^2. \tag{8}$$

When $\sin i < 1$, the mass inferred from Eq. (7) under the edge-on assumption is interpreted as the minimum mass $M_p \sin i$; the general amplitude formula appears in Appendix A.

2.3 Parameter estimation

Let $\{t_j, v_j, \sigma_j\}$ denote the observed times, radial velocities, and uncertainties. We minimize the weighted residual sum of squares

$$\chi^2(\boldsymbol{\theta}) = \sum_j \left(\frac{v_j - v_r(t_j; \boldsymbol{\theta})}{\sigma_j} \right)^2, \tag{9}$$

with parameter vector $\boldsymbol{\theta} = (K, P, e, \omega, t_0, \gamma)$.

Because χ^2 is nonconvex in the orbital elements, we first perform a global search with differential evolution [9, 11], which maintains a population of candidate solutions and updates them by mutation and crossover. The best candidate is then polished with a bounded nonlinear least-squares solver [11]. Search bounds are constructed from the observation baseline and the observed velocity span, with $0 \le e \le 0.85$ to avoid near-parabolic degeneracies; numerical settings and per-series bounds are listed in Appendix D. For the synthetic validation run we also record the best-so-far χ^2 after each differential-evolution generation (Figure 6).

2.4 Orbit visualization

After fitting, we construct barycentric initial conditions consistent with the derived a, e, and component masses, and integrate the Newtonian two-body problem with the velocity Verlet algorithm [12]. This integration is used solely for visualization of the reflex orbit; it is not part of the likelihood evaluation. The explicit initial-condition and update equations are given in Appendix A.

3 Data

3.1 Synthetic validation set

To quantify recovery accuracy we generate a synthetic RV series for a Jupiter-class companion around a $\sim 1.08\,M_\odot$ star with planted parameters

$$P = 147.5\,\mathrm{d}, \quad K \approx 30.5\,\mathrm{m\,s^{-1}}, \quad e = 0.19,$$
$$\omega = 1.05\,\mathrm{rad}, \quad t_0 = 18.0\,\mathrm{d}, \quad \gamma = 4.5\,\mathrm{m\,s^{-1}}, \quad M_p = 0.82\,M_J.$$

Observation times are drawn irregularly over a 420 d window. Independent Gaussian measurement noise of standard deviation $\sigma_\mathrm{n} = 2.2\,\mathrm{m\,s^{-1}}$ and an independent Gaussian jitter draw of standard deviation $\sigma_\mathrm{jit} = 0.7\,\mathrm{m\,s^{-1}}$ are added to each sample (Appendix A).

3.2 Observational Doppler series

We analyze four observational Doppler-shift time series (`star0`–`star3`) with host masses 1.11, 1.39, 2.30, and $1.34\,M_\odot$, respectively. Times are recorded in seconds and converted to days; Doppler shifts are converted to radial velocities as described above. In the absence of published per-point uncertainties we adopt a uniform $\sigma = 1\,\mathrm{m\,s^{-1}}$ for weighting.

Data provenance. These observational files were provided by the author's independent research mentor and are understood to originate from a public NASA exoplanet/radial-velocity archive. The specific catalog, survey program, or DOI associated with each series was not retained with the working copies used here, so we treat the files as anonymized archival Doppler time series

rather than as named discoveries. The analysis below should therefore be read as a methodological demonstration on publicly sourced RV-like data, not as a claim of new planet discovery or a re-reduction of a particular NASA data release.

4 Results

4.1 Synthetic recovery

Table 1 compares planted and recovered parameters. The period and semi-amplitude are recovered to within $\sim 3\%$, and the residual RMS (Appendix A) is $2.11\,\mathrm{m\,s^{-1}}$, consistent with the injected noise level. Figure 1 shows the observations, the best-fit Keplerian curve, the ground-truth curve, and the corresponding barycentric orbit.

Table 1: Synthetic validation: planted truth versus recovered fit.

Quantity	Truth	Fit	Relative error
P (d)	147.5	147.16	0.2%
K ($\mathrm{m\,s^{-1}}$)	30.51	31.35	2.8%
e	0.190	0.221	—
M_p (M_J)	0.820	0.836	2.0%
RMS ($\mathrm{m\,s^{-1}}$)	—	2.11	—

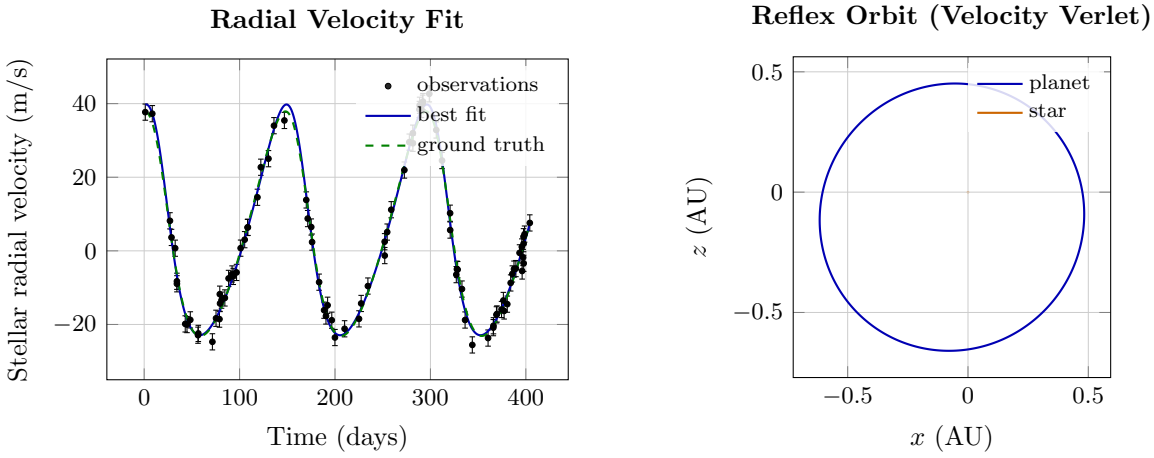

Figure 1: Synthetic radial-velocity fit. Left: noisy observations (points), best-fit Keplerian model (solid), and planted ground truth (dashed). Right: barycentric star–planet orbit integrated with velocity Verlet from the fitted elements.

4.2 Observational fits for `star0`–`star3`

Table 2 summarizes the best-fit Keplerian parameters for all four observational series. Figure 2 shows the cleanest recovery (`star0`); the remaining RV and orbit panels appear in Appendix B, and the full six-element solutions are collected in Appendix C.

`star0` yields a short-period, nearly circular solution with coherent phase coverage over $\sim 14\,\mathrm{d}$ and residual RMS $5.23\,\mathrm{m\,s^{-1}}$. Under the edge-on assumption the companion mass is $M_p \sin i \approx$

$0.49\,M_J$ at $a \approx 0.053\,\mathrm{AU}$.

`star2` and `star3` recover longer-period solutions ($P \sim 10^3\,\mathrm{d}$) with residual RMS of 14.4 and $8.5\,\mathrm{m\,s^{-1}}$, respectively. `star2` is nearly circular ($e \approx 0.06$), while `star3` is moderately eccentric ($e \approx 0.59$).

`star1` is the most challenging series: the best single-Keplerian model returns a long, highly eccentric orbit ($P \approx 3030\,\mathrm{d}$, $e \approx 0.83$) but leaves a large residual RMS of $314\,\mathrm{m\,s^{-1}}$ (Figure 3). That outcome indicates that a single-planet Keplerian description is inadequate for this time series under the present noise model—possible explanations include incomplete phase coverage of a long-period orbit, additional companions, stellar activity, or unmodeled instrumental systematics [5, 8]. We report the fit for completeness while treating it as a negative control rather than a robust orbital solution.

Table 2: Best-fit single-planet Keplerian parameters for the four observational Doppler series. Masses assume $\sin i = 1$. Full orbital elements are given in Table 4.

Quantity	`star0`	`star1`	`star2`	`star3`
N points	32	98	51	44
$M_\star$ ($M_\odot$)	1.11	1.39	2.30	1.34
P (d)	4.269	3029.7	991.9	986.7
K ($\mathrm{m\,s^{-1}}$)	56.69	352.7	119.8	93.88
e	0.002	0.832	0.064	0.587
γ ($\mathrm{m\,s^{-1}}$)	9.40	−18.76	−0.30	41.56
a (AU)	0.053	4.591	2.573	2.141
$M_p \sin i$ (M_J)	0.485	17.50	10.26	4.534
RMS ($\mathrm{m\,s^{-1}}$)	5.23	313.9	14.36	8.50

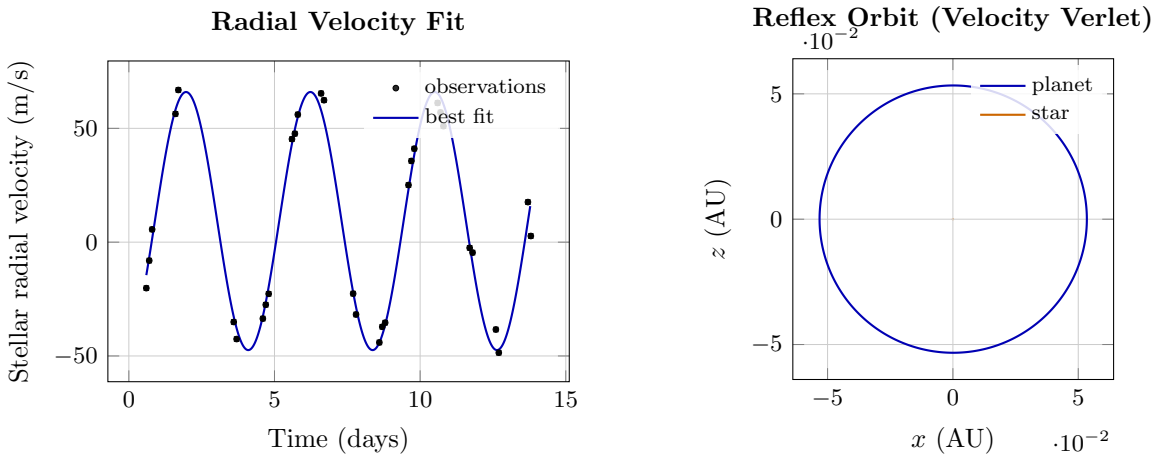

Figure 2: Keplerian fit to the `star0` Doppler observations. Left: radial-velocity time series and best-fit model. Right: corresponding barycentric orbit. Fits for `star1`–`star3` are shown in Appendix B.

5 Discussion

The synthetic experiment confirms that differential evolution followed by local refinement is sufficient to recover the dominant Keplerian parameters when the noise is Gaussian and the sampling

covers multiple orbital cycles [3, 9]. Eccentricity is the most weakly constrained element in our synthetic run, as expected when the signal-to-noise ratio is modest and the true e is moderate [8].

Across the observational sample, `star0` behaves like a compact, low-eccentricity RV signal of the kind first revealed by early Doppler surveys [1]. `star2` and `star3` illustrate longer-period recoveries with acceptable residuals, while `star1` demonstrates a clear failure mode of the single-planet model. Several caveats apply to all four fits. First, the adopted uncertainties are uniform and may not reflect the true error budget, so formal χ^2 values should not be over-interpreted. Second, the masses we report are $M_p \sin i$; without an independent inclination constraint the true masses may be larger. Third, the model assumes a single planet and a constant systemic velocity, omitting stellar activity, instrumental offsets, and additional companions [5]. Fourth, because the specific NASA archive identifiers were not retained with the working files, these results are best viewed as pipeline validation on archival Doppler series rather than as definitive orbital solutions for named systems.

Natural extensions include periodogram-based period initialization [4], multi-planet Keplerian models [3], and Bayesian posterior sampling for full uncertainty quantification [8].

6 Conclusions

We have described a Keplerian radial-velocity pipeline for single-planet parameter estimation. The method combines an analytic RV forward model, differential-evolution global search, and least-squares refinement, with derived planet mass and semi-major axis under the edge-on limit. Synthetic tests recover K and P to within a few percent. Application to four observational Doppler series recovers a short-period circular solution, two longer-period companions with moderate residuals, and one series for which a single Keplerian model is clearly inadequate. The accompanying open-source implementation provides a reproducible basis for further methodological development.

Acknowledgments

The author thanks his independent research mentor for providing the observational Doppler time series used in this study. Those data are understood to have been drawn from a public NASA exoplanet/radial-velocity archive; the specific catalog identifiers were not retained with the working copies analyzed here.

Software

The analysis is implemented in Python using NumPy, SciPy [11], and Matplotlib. Source code and example scripts are available in the project repository accompanying this manuscript. Commands used to regenerate the paper figures are listed in Appendix E.

A Notation and supplementary definitions

Symbols

Unless noted otherwise, times are expressed in days in the fitting interface and converted to seconds only when evaluating Newtonian formulas that involve G. Masses $M_\odot$ and M_J denote one solar mass and one Jupiter mass, respectively. The Doppler observables use rest wavelength λ and

observed wavelength shift $\Delta\lambda$, so that $z = \Delta\lambda/\lambda$. The fitted velocities v_j are identified with the line-of-sight speed v obtained from z.

The orbital inclination i is the angle between the orbital angular-momentum vector and the line of sight, so that an edge-on orbit has $i = 90^\circ$ and $\sin i = 1$. The relative orbital semi-major axis a is the semi-major axis of the planet–star separation vector.

General semi-amplitude

Allowing for arbitrary inclination, Eq. (7) generalizes to

$$K = \left(\frac{2\pi G}{P}\right)^{1/3} \frac{M_p \sin i}{(M_\star + M_p)^{2/3}} \frac{1}{\sqrt{1-e^2}}, \tag{10}$$

with P in seconds when G is in SI units. Inverting Eq. (7) with $\sin i = 1$ therefore returns $M_p \sin i$ whenever the true inclination is unknown.

Residual diagnostics

For N observations the unweighted residual root-mean-square reported in the tables is

$$\mathrm{RMS} = \sqrt{\frac{1}{N}\sum_{j=1}^{N}\bigl(v_j - v_r(t_j;\hat{\boldsymbol{\theta}})\bigr)^2}, \tag{11}$$

where $\hat{\boldsymbol{\theta}}$ is the best-fit parameter vector. This is distinct from the weighted objective $\chi^2(\boldsymbol{\theta})$ used during optimization. Relative errors in validation tables are $|\hat{q} - q_{\mathrm{true}}|/|q_{\mathrm{true}}|$ for a scalar quantity q.

Synthetic noise model

Synthetic observations are generated as

$$v_j = v_r(t_j;\boldsymbol{\theta}_{\mathrm{true}}) + \varepsilon_{\mathrm{n},j} + \varepsilon_{\mathrm{jit},j}, \tag{12}$$

where $\varepsilon_{\mathrm{n},j} \sim \mathcal{N}(0,\sigma_{\mathrm{n}}^2)$ and $\varepsilon_{\mathrm{jit},j} \sim \mathcal{N}(0,\sigma_{\mathrm{jit}}^2)$ are independent. The fitting weights use $\sigma_j = \sigma_{\mathrm{n}}$ and therefore do not include the jitter variance. For the archived series we likewise adopt a uniform $\sigma_j = 1\,\mathrm{m\,s^{-1}}$ in the absence of published uncertainties.

Orbit visualization

Orbit panels show barycentric trajectories in an orbital x–z plane with the line-of-sight direction along $+z$. Given relative polar radius

$$r = \frac{a(1-e^2)}{1 + e\cos\nu} \tag{13}$$

and argument of periastron ω, the planet–star relative state in that plane is obtained by rotating the perifocal vectors through ω. Barycentric positions and velocities then follow from the mass ratio $\mu_p = M_p/(M_\star + M_p)$,

$$\mathbf{r}_\star = -\mu_p\,\mathbf{r}, \qquad \mathbf{r}_p = (1-\mu_p)\,\mathbf{r}, \tag{14}$$

and likewise for the velocities. Starting from those initial conditions, the Newtonian accelerations

$$\ddot{\mathbf{r}}_\star = GM_p \, \frac{\mathbf{r}_p - \mathbf{r}_\star}{|\mathbf{r}_p - \mathbf{r}_\star|^3}, \qquad \ddot{\mathbf{r}}_p = -GM_\star \, \frac{\mathbf{r}_p - \mathbf{r}_\star}{|\mathbf{r}_p - \mathbf{r}_\star|^3} \tag{15}$$

are integrated with the velocity Verlet update

$$\begin{aligned} \mathbf{r}(t + \Delta t) &= \mathbf{r}(t) + \mathbf{v}(t)\,\Delta t + \tfrac{1}{2}\mathbf{a}(t)\,(\Delta t)^2, \\ \mathbf{v}(t + \Delta t) &= \mathbf{v}(t) + \tfrac{1}{2}\big(\mathbf{a}(t) + \mathbf{a}(t + \Delta t)\big)\Delta t. \end{aligned} \tag{16}$$

The visualization uses a fixed number of steps over one fitted orbital period and does not enter the RV likelihood.

B Additional observational figures

Figures 3–5 show the RV fits and barycentric orbits for the three longer-baseline observational series discussed in the main text.

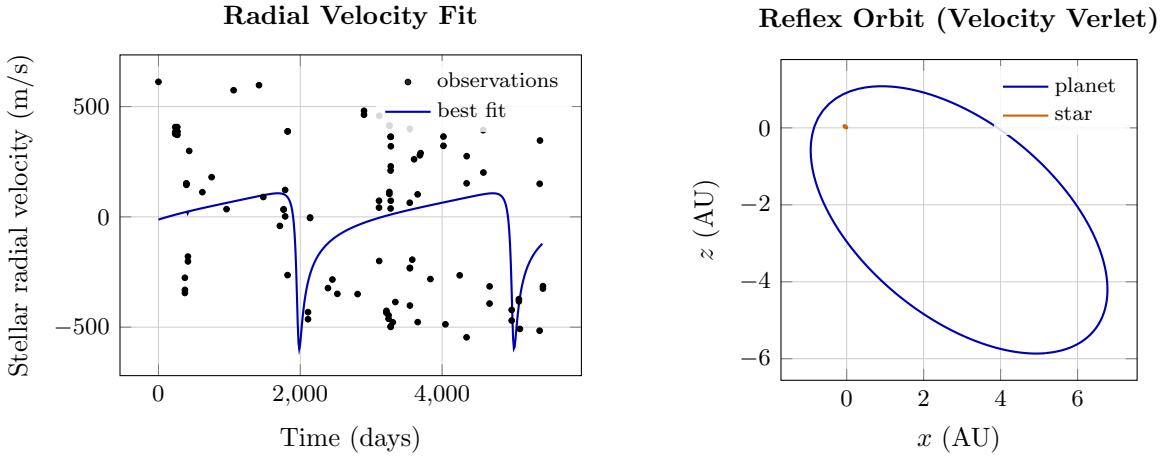

Figure 3: Best single-Keplerian fit to `star1`. The large residual RMS indicates that this series is not well described by a single companion under the present model assumptions.

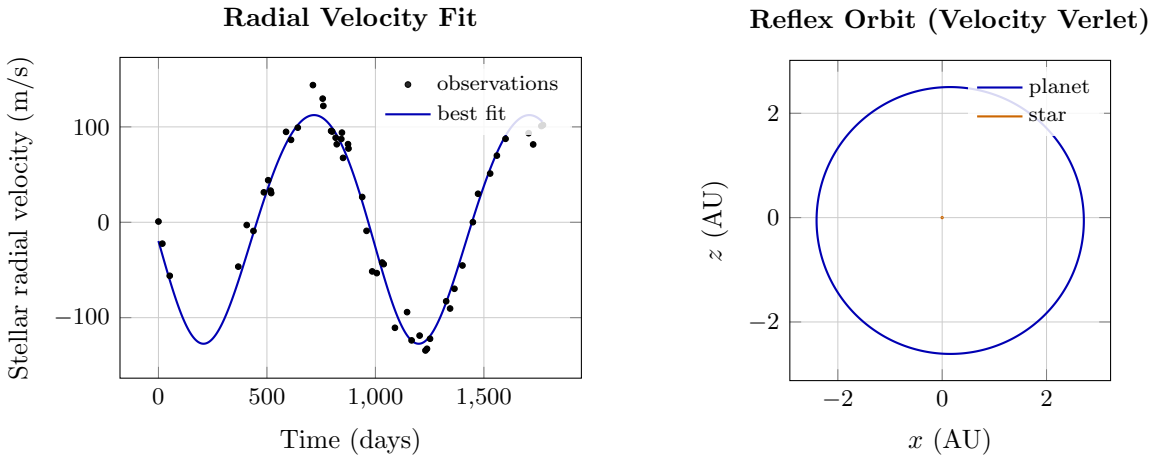

Figure 4: Keplerian fit to the `star2` Doppler observations.

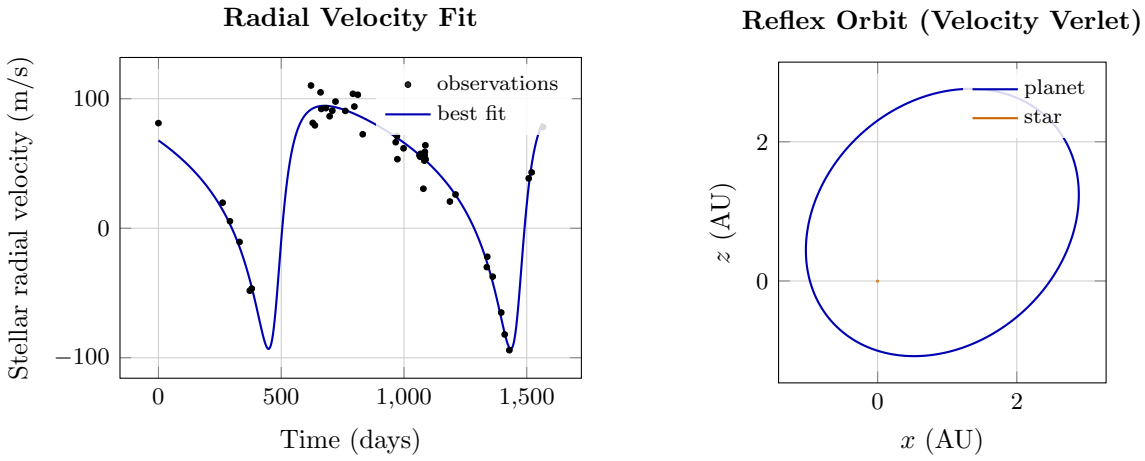

Figure 5: Keplerian fit to the `star3` Doppler observations.

C Full Keplerian solutions

Table 3 reports all six fitted Keplerian elements for the synthetic validation run. Table 4 lists the corresponding solutions for `star0`–`star3`. Times of periastron are reported in the same day units as the input time series and need not fall inside the observational window because the mean anomaly is 2π-periodic.

Table 3: Full synthetic Keplerian solution (planted truth versus recovered fit).

Parameter	Truth	Fit	Relative error
K ($\mathrm{m\,s^{-1}}$)	30.51	31.35	2.8%
P (d)	147.5	147.16	0.2%
e	0.190	0.221	—
ω (rad)	1.050	1.000	—
t_0 (d)	18.0	459.0	—
γ ($\mathrm{m\,s^{-1}}$)	4.50	4.68	—
M_p (M_J)	0.820	0.836	2.0%
a (AU)	—	0.560	—
RMS ($\mathrm{m\,s^{-1}}$)	—	2.11	—
χ^2	—	84.9	—

Table 4: Full single-planet Keplerian solutions for the observational series. Masses assume $\sin i = 1$.

Parameter	`star0`	`star1`	`star2`	`star3`
K ($\mathrm{m\,s^{-1}}$)	56.69	352.7	119.8	93.88
P (d)	4.269	3029.7	991.9	986.7
e	0.0023	0.832	0.064	0.587
ω (rad)	−2.883	2.456	2.798	−2.407
t_0 (d)	−4.265	−4092	159.9	−1499
γ ($\mathrm{m\,s^{-1}}$)	9.40	−18.76	−0.30	41.56
a (AU)	0.0533	4.591	2.573	2.141
$M_p \sin i$ (M_J)	0.485	17.50	10.26	4.534
RMS ($\mathrm{m\,s^{-1}}$)	5.23	313.9	14.36	8.50
χ^2	875	9.65×10^6	1.05×10^4	3177

D Optimizer configuration

The global stage uses SciPy's differential-evolution routine with `polish=False`, `updating=deferred`, a fixed random seed, and at most 300 iterations for the synthetic run (400 for the observational series). The local stage is SciPy's bounded nonlinear least-squares solver applied to the weighted residual vector, with a budget of 2×10^4 function evaluations. The free parameter vector is ordered as $(K, P, e, \omega, t_0, \gamma)$.

Figure 6 shows the synthetic-run convergence trace: the best population χ^2 after each differential-evolution generation, the final least-squares polish, and the relative errors in K and P against the planted truth. Early generations reduce χ^2 by orders of magnitude; once P is approximately recovered, further improvement is comparatively gradual before the local polish.

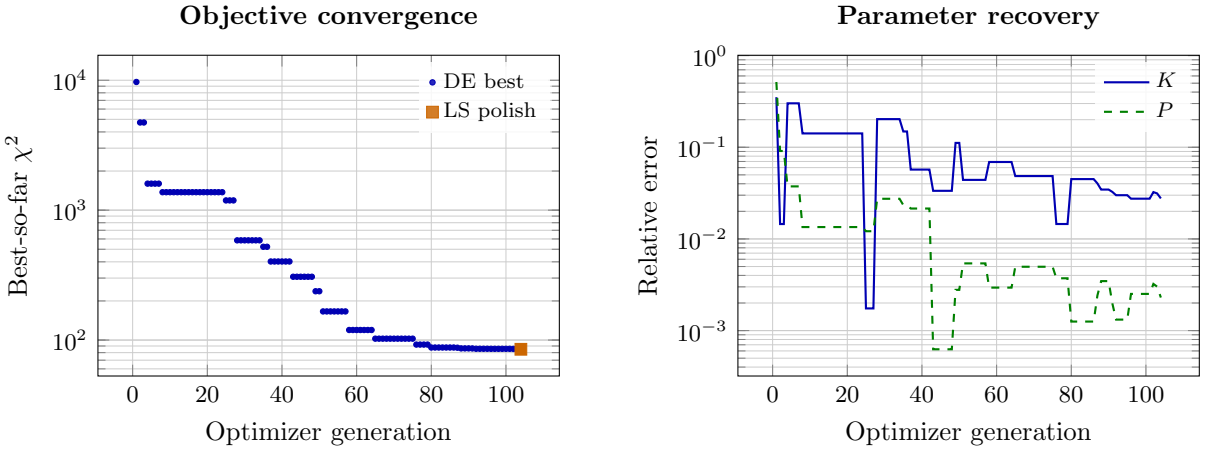

Figure 6: Synthetic optimizer convergence. Left: best-so-far weighted χ^2 after each differential-evolution generation (circles) and after the final least-squares polish (square). Right: relative errors in the recovered semi-amplitude K and period P versus the planted truth.

For the synthetic dataset the default bound construction of the package is used. For the archived series we adopt slightly wider amplitude and period windows keyed to the observed velocity span and baseline, with an expanded period upper limit of 6000 d for `star1`. In all cases $0 \le e \le 0.85$

and $-\pi \leq \omega \leq \pi$. Table 5 lists the numerical bounds used for each fit.

Table 5: Search bounds used for each fit. Units are $\mathrm{m\,s^{-1}}$ for K and γ, days for P and t_0, and radians for ω.

Series	K	P	e	ω	t_0	γ
Synthetic	[1, 102]	[50.4, 604]	[0, 0.85]	$[-\pi, \pi]$	[−603, 606]	[−107, 97]
`star0`	[1, 231]	[0.75, 15.8]	[0, 0.85]	$[-\pi, \pi]$	[−15.2, 16.4]	[−223, 238]
`star1`	[1, 2316]	[136, 6506]	[0, 0.85]	$[-\pi, \pi]$	[−6506, 6506]	[−2317, 2315]
`star2`	[1, 556]	[44.3, 2127]	[0, 0.85]	$[-\pi, \pi]$	[−2127, 2127]	[−541, 571]
`star3`	[1, 409]	[39.1, 1879]	[0, 0.85]	$[-\pi, \pi]$	[−1879, 1879]	[−365, 452]

E Reproducibility commands

From the project root, regenerate the CSV tables and light-theme vector PDFs, then compile this manuscript, with

```
MPLBACKEND=Agg uv run python examples/export_paper_figures.py
latexmk -pdf -cd docs/exoplanet_showcase_report.tex
```

Print figures in the PDF are drawn natively with PGFPlots from the exported CSV tables under `docs/figures/plotdata/`. The same export script also writes Matplotlib PDF copies under `docs/figures/`.

References

[1] Michel Mayor and Didier Queloz. A Jupiter-mass companion to a solar-type star. *Nature*, 378 (6555):355–359, 1995. doi: 10.1038/378355a0.

[2] Geoffrey W. Marcy and R. Paul Butler. A planetary companion to 70 Virginis. *The Astrophysical Journal Letters*, 464:L147–L151, 1996. doi: 10.1086/310096.

[3] J. T. Wright and A. W. Howard. Efficient fitting of multiplanet Keplerian models to radial velocity and astrometry data. *The Astrophysical Journal Supplement Series*, 182(1):205–215, 2009. doi: 10.1088/0067-0049/182/1/205.

[4] Andrew Cumming. Detectability of extrasolar planets in radial velocity surveys. *Monthly Notices of the Royal Astronomical Society*, 354(4):1165–1176, 2004. doi: 10.1111/j.1365-2966.2004.08275.x.

[5] Debra A. Fischer et al. Exoplanet detection techniques. *Protostars and Planets VI*, pages 715–737, 2014. doi: 10.2458/azu_uapress_9780816531240-ch031.

[6] Carl D. Murray and Stanley F. Dermott. *Solar System Dynamics*. Cambridge University Press, 1999. doi: 10.1017/CBO9781139174817.

[7] C. D. Murray and A. C. M. Correia. Keplerian orbits and dynamics of exoplanets. In Sara Seager, editor, *Exoplanets*, pages 15–23. University of Arizona Press, 2010.

[8] Eric B. Ford. Quantifying the uncertainty in the orbits of extrasolar planets. *The Astronomical Journal*, 129(3):1706–1717, 2005. doi: 10.1086/427962.

[9] Rainer Storn and Kenneth Price. Differential evolution – a simple and efficient heuristic for global optimization over continuous spaces. *Journal of Global Optimization*, 11(4):341–359, 1997. doi: 10.1023/A:1008202821328.

[10] L. Lindegren and D. Dravins. The fundamental definition of "radial velocity". *Astronomy & Astrophysics*, 401:1185–1201, 2003. doi: 10.1051/0004-6361:20030181.

[11] Pauli Virtanen et al. SciPy 1.0: fundamental algorithms for scientific computing in Python. *Nature Methods*, 17:261–272, 2020. doi: 10.1038/s41592-019-0686-2.

[12] Loup Verlet. Computer "experiments" on classical fluids. I. Thermodynamical properties of Lennard-Jones molecules. *Physical Review*, 159(1):98–103, 1967. doi: 10.1103/PhysRev.159.98.